Experimental and numerical investigation on the flow and heat transfer behaviors during a compression–cooling–expansion cycle using a liquid piston for compressed air energy storage

El Mehdi Gouda, Thibault Neu, Mustapha Benaouicha, Yilin Fan, Albert Subrenat, Lingai Luo

Experimental and numerical investigation on the flow and heat transfer behaviors during a compression-cooling-expansion cycle using a liquid piston for compressed air energy storage

El Mehdi GOUDA[a,b], Thibault NEU[a,c], Mustapha BENAOUICHA[a,*], Yilin FAN[b], Albert SUBRENAT[c], Lingai LUO[b,*]

[a]*Segula Technologies. Naval and Energy Engineering Research and Innovation Unit. 9 avenue Edouard Belin, 92500 Rueil-Malmaison, France*
[b]*Nantes Université, CNRS, Laboratoire de Thermique et Énergie de Nantes, LTeN, UMR 6607, F-44000 Nantes, France*
[c]*IMT Atlantique, GEPEA UMR CNRS 6144, 4 Rue Alfred Kastler, 44000 Nantes, France*

Abstract

This paper investigates flow patterns and heat transfer characteristics inside the Liquid Piston (LP) column during a complete compression-cooling-expansion (CCE) cycle. The phenomena associated to this cycle have not been yet well-documented but are essential to understand the transfer mechanisms for piston geometry optimization. A 3D CFD model based on VOF method and the Particle Image Velocimetry (PIV) technique have been performed to study the CCE cycle. Different air flow patterns and transition as well as the temperature field at different stages of the cycle have been visualized, analyzed, compared and discussed. During the expansion stage, a fast establishment of an axisymmetric flow structure, its evolution and disruption to a totally chaotic one can be identified. Under the tested piston speed (0.033 $m.s^{-1}$) and compression/expansion ratio (*CR=ER=4.8*), a close-to-isothermal cycle could be realized by the LP, with high compression, expansion and overall efficiencies (up to $\eta_c = 91.2\%$, $\eta_e = 94.7\%$ and $\eta_{cycle} = 86.3\%$), confirming the interests of LP in realizing

DOI: `https://doi.org/10.1016/j.energy.2023.127622`
*Corresponding author
Email addresses: `mustapha.benaouicha@segula.fr` (Mustapha BENAOUICHA), `lingai.luo@univ-nantes.fr` (Lingai LUO)

Isothermal-CAES systems. Results of a numerical parametric study show that a lower wall temperature could slightly enhance both the compression and expansion efficiencies while a slow piston speed is rather beneficial for a high overall efficiency.

Keywords: Compressed air energy storage (CAES); Liquid Piston (LP); Compression-cooling-expansion (CCE) cycle; Flow and heat transfer behaviors; Particle Image Velocimetry (PIV); Efficiency

---

Nomenclature

Abbreviations

CAES	Compressed Air Energy Storage
CCE	Compression-Cooling-Expansion
CFD	Computational Fluid Dynamics
CR	Compression Ratio
ER	Expansion Ratio
LP	Liquid Piston
VOF	Volume Of Fluid

Greek Symbols

η	Efficiency
γ	Polytropic coefficient
λ	Thermal conductivity ($W.m^{-1}K^{-1}$)
μ	Dynamic viscosity ($N.m^{-2}$)
ν	Kinematic viscosity ($m^2.s$)

ρ	Density ($kg.m^{-3}$)

Non-dimensional numbers

Co	Courant number
Re	Reynolds number

Latin symbols

c	Specific heat capacity ($J.kg^{-1}.K^{-1}$)
D	Diameter (m)
E	Energy (J)
L	Length (m)
m	Mass (kg)
P	Pressure (Pa)
r	Ideal gas constant ($J.Kg^{-1}.K$)
T	Temperature (K)
t	Time (s)
U	Velocity ($m.s^{-1}$)
W	Work (J)

Subscripts

0	Initial at $t = 0s$
air	Air
ave	Average
c	Compression
cool	Cooling

$cycle$	Compression-cooling-expansion cycle
D	Diameter
e	Expansion
exp	Experimental
f	Final at $t = t_f$
k	Kinematic
p	Potential
$pist$	Piston
ref	Reference
$walls$	Wall
$water$	Water

1. Introduction

The continuous increase of electricity consumption by households and industries under the 2050 carbon-neutral target has led to the growing share of renewable energy sources to replace the fossil fuels [1]. In this context, energy storage technologies have been developed to overcome the intermittency issue of these clean energy sources, providing ancillary services to the electricity grid [2]. Over the past decades, the compressed air energy storage (CAES) systems have attracted increasing attention due to their cost-effective electricity storage at large-scale, high storage capacity, low self-discharge, and long lifetime [3, 4, 5, 6, 7].

The efficiency and storage capacity of the CAES systems could be strongly impacted by the air temperature evolution during the compression or expansion operation [8, 9]. To overcome this problem, the new generations of CAES technology aim to reduce the temperature evolution during the storage and

regeneration operations and thus approach the isothermal cyclic operations (I-CAES) [10, 8]. In this context, the liquid piston (LP) concept is considered as a promising alternative to the existing solid piston solutions due to more efficient thermal management [11]. For this concept, a liquid (often water) is used to replace the solid piston to reciprocally compress and expand the gas (often air), avoiding the leakage problem while largely reducing the friction loss. Moreover, the strong thermal management capacity of LP renders high efficiency of the cycle, i.e., up to 95% compressor/expander efficiency as well as 70% round-trip efficiency (RTE) of the cycle could be achieved by LP, demonstrating the great interest in the development and deployment of this technology for I-CAES [12, 13, 14].

Numerous studies have been conducted to better characterize the compression/expansion processes using the LP, as outlined in a recent review paper [8]. Some studies [15, 16, 17, 18] investigated the influences of operating conditions on the compression/expansion efficiency of the LP by thermodynamic analysis. Others [19, 20, 21, 22] proposed and implemented different heat transfer enhancement measures for better thermal management, in order to approach the isothermal cycle. The average temperature and pressure of the gas phase are usually monitored and analysed in experimental studies. While most of the studies on this topic focus on the LP compression, the expansion process is relatively less investigated, and those on complete compression-cooling-expansion (CCE) cycles for real LP operation are still rare. Some experimental and numerical studies involving expansion process or a CCE cycle using LP (or solid piston) are listed in Table 1.

Török et al. [23] studied the energy conversion process of a quasi-isothermal air compression and expansion of a LP through a thermodynamic modeling. The advantages of LP over a conventional solid piston system have been put forward. The expansion process of a LP was studied by Zhang et al. [24] by means of 2D computational fluid dynamics (CFD) simulation and by experimental measurement of the global air temperature (using an inverse method). The concepts with and without honeycomb-like metal foam inserts were stud-

ied and compared. For LP column without metal foam insert, a slow piston speed at the beginning of the expansion is beneficial to avoid the significant volume change (and thus heat release). In contrast, a fast piston speed at the beginning of the expansion is recommended for the LP with inserts owing to the enhanced thermal management capacity. Yan et al. [25] performed an experimental study to compare the effects of different porous media in a LP during compression/expansion operations. Their results showed that, while the impacts of these inserts on the efficiency could be noticeable, a close-to-isothermal operation cycle could be realized by LP. Later on, Wieberdink et al. [26] extended the study to a higher pressure range ($210 \cdot 10^5\, Pa$). Recently, Li et al. [27] conducted an analytical and experimental study for a large-scale LP ($V = 24.71\, m^3$) applied to Hydro-pneumatic Energy Storage (HYPES). A four-stages processes cycle (Inhalation-Compression-Expansion-Exhaust) has been studied, each cycle lasting more than 1 hour for a $CR = 11$ and $\Delta T_{air,ave} > 90\, K$. The exergy efficiency at 86.4% has been reported for the compression stage.

The above literature survey shows that both the experimental and numerical studies on the flow and heat transfer characteristics at local level inside the LP column are still limited. Noteworthy is the experimental study of Neu & Subrenat [28], in which the air flow patterns inside the piston column during compression operation have been visualized using Particle Image Velocimetry (PIV) technique. This study has been complemented recently by a 3D CFD simulation using VOF model [29], providing detailed information on the presence and transition between different flow patterns, and the conjugated heat transfer. Nevertheless, to the best of our knowledge, no such study exists in the literature on the local fluid low and heat transfer behaviors during the expansion operation, letting alone the complete CCE cycle by LP.

The aim of this study is to fill this research gap by investigating the flow and heat transfer behaviors inside a LP during a complete cycle composed of air compression, cooling and air expansion (CCE cycle). The present study completes our earlier works focusing on the LP compression by investigating the whole CCE cycle, using the experimental setup of Neu et al. [28] and numerical

Study	Year	Type	L/D	CR	Working fluids	Methodology	Main findings	Notes
Van de Ven & Li [11]	2009	Num. + Exp.	44	9.5	Air/water	Simplified numerical model $Re_{water} = 300$	100 K air temperature increase	50000 small cylinder inserts
Kim and Favrat [30]	2010	Num.	–	7-50	Air/water	Energy and exergy analysis	Two stages system increases η_c by 4%	Modeling of the overall efficiency of a micro-CAES
Török et al. [23]	2013	Exp.	1.33	7.3	Air/water	Simplified thermodynamic model	Comparison between solid and liquid piston	Advantages of liquid piston highlighted
Yan et al. [25]	2015	Exp.	6	13	Air/water	Inverse method for temperature calculation	Noticeable effects of geometry and position of the inserts on the efficiency	Porous media; compression & expansion operations
Odukomaiya et al. [15]	2016	Num. + Exp.	–	1.8	Air/water	Global thermodynamic model	3 different cycles + spray cooling	Large scale compression & expansion
Wieberdink et al. [26]	2018	Exp.	6.35	30	Air/water	Inverse method for temperature calculation	Noticeable effects of geometry and position of the inserts on the efficiency	Porous media; compression & expansion operations
Ahn et al. [21]	2021	Exp.	3.2	2.8	Air/water	Thermodynamic model	Effects of spray injection and metal wire insert	Successive compression/expansion
Yu and al. [31]	2022	Exp.	1	8	Air/Solid piston	Correlations for heat transfer modeling	Significant effect of spray injection on the cooling	-
Li et al. [27]	2022	Exp.	3	1.8-10	Air/water	Local temperature measurement by 5 temperature detectors	Four stages cycle Inhale-compress-exhaust-expand	Very slow piston speed; pilot-scale LP
Neu & Subrenat [28]	2021	Exp.	35	5	Air/solid piston	PIV	Air flow inside piston visualized during slow compression	Previous study of compression
Gouda et al. [29]	2022	Num.	35	5	Air/water	3D CFD VOF method	Air flow characterisation during compression	Previous study on LP compression

Table 1: Experimental and numerical studies on the compression-expansion cycle by LP

model of Gouda et al. [29]. Different air flow patterns and its evolution during the complete cycle were visualized, and the conjugated heat transfer inside the LP column were analysed in detail for the first time. The compression, expansion and the overall efficiencies of the cycle were calculated as well to highlight the advantages of the LP for CAES. The numerical and experimental results presented in this paper may provide a better understanding of the physical phenomena of air compression/expansion cycle by LP on one hand, and identify the performance improvement pathways to approach the I-CAES on the other hand.

The rest of the paper is organized as follows. The studied CCE cycle as well as the LP geometry and operating conditions are presented in section 2. The numerical and experimental methodologies are described in detail in section 3. Section 4 presents a comparison of the numerical and experimental results with the purpose of validating the model. Later in section 5, the flow and heat transfer characteristics in the LP column during the CCE cycle are reported and analysed. A numerical parametric study is reported in section 6, to show the effects of LP operating parameters on the efficiency of each process. Finally in section 7, main conclusions of the study are summarized.

2. Studied cycle and the LP column

2.1. Compression-Cooling-Expansion (CCE) cycle

The storage/restitution cycle of a real LP-based CAES system is composed of several stages. During the charging/storage phase, the air is firstly compressed by LP and then injected into the air storage tanks at high pressure. During the discharging/restitution phase, the piston valve is firstly opened to bring a certain amount of compressed air into the LP column. After closing the valve, the expansion process starts. The expanded air pushes the water through a turbine to regenerate electricity.

A relatively simpler cycle is investigated in this work, equivalent to a reversed Stirling cycle [32]. It involves a closed LP chamber (introduced in detail in

section 2.2), in which the air is first compressed from P_0 to P_c at a piston speed of $U_{pist,c}$. Despite the cooling effect by LP, a higher air temperature ($T_c > T_0$) would be resulted at the end of compression. This amount of air stays then at the top of the piston to undergo an isochoric cooling at $U_{pist} = 0$, representing the status of air storage in the tanks. When the air temperature returns to its initial temperature (T_{cool}; P_{cool}), the expansion process starts at a piton speed of $U_{pist,e}$. At the end of the CCE cycle, the air-water interface inside the column is at the same position as in the initial one, i.e. air's final volume V_f is equal to the initial one V_0. The operating parameters for each phase of the cycle are given in Fig. 1 and Table 2.

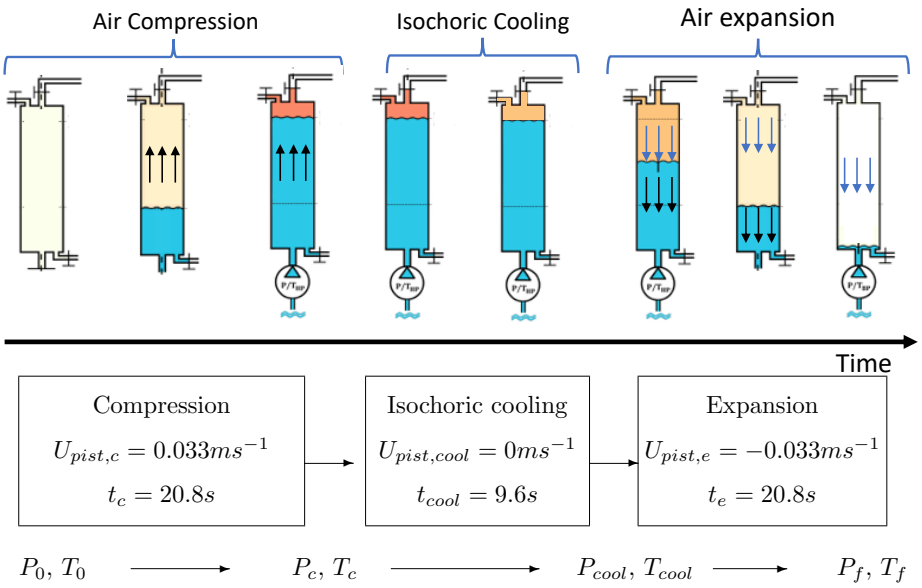

Figure 1: The studied air compression-isochoric cooling-expansion (CCE) cycle in a LP column

2.2. Geometry and dimensions of the LP column

The same LP geometry without inserts is tested both in experiments and in simulation. Air is used as the gas phase while water is used as the liquid. It is a simple cylinder with $L_0 = 0.906\,m$ in length and $D = 0.0518\,m$ in diameter.

Figure 2 shows a schematic view of the LP column and the position of the piston at the beginning of each phase. Note that L_{pist} denotes the piston position (air-water interface) at time t, R^* is the normalized radial position ($R^* = [-1; 1]$) and L_z^* is the normalized longitudinal position ($L_z^* = [0; 1]$). The column walls are all considered at constant temperature of $T_{walls} = 300\,K$ (isothermal wall condition).

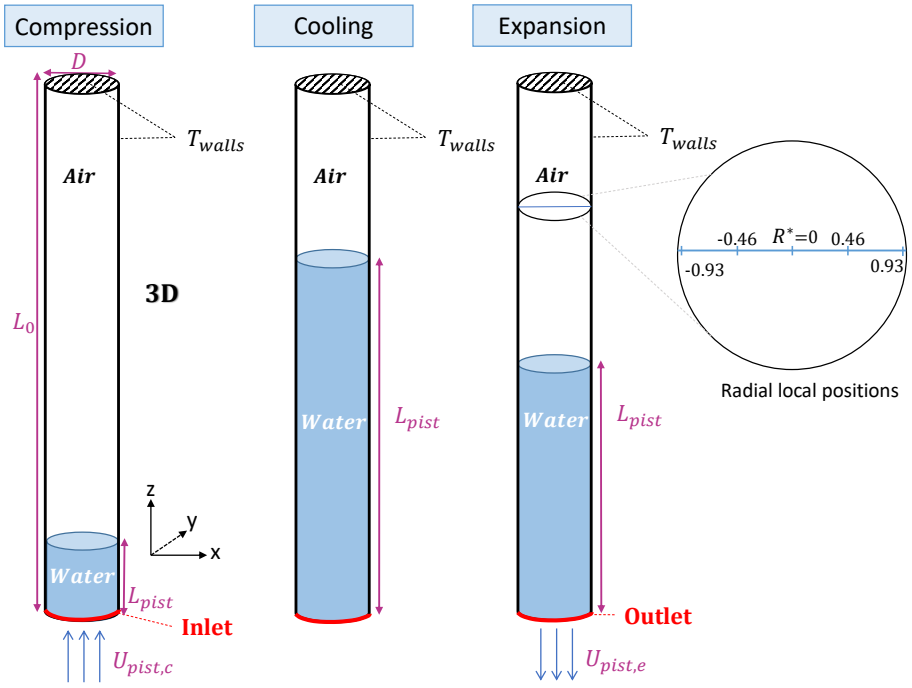

Figure 2: LP geometry, boundary conditions and piston position at each stage of the studied CCE cycle

3. Numerical and experimental methodologies

In this section, the numerical models and parameters for the 3D simulation of LP CCE cycle will be presented in detail. In parallel, the experimental setup and PIV measurement facilities will also be introduced.

3.1. Numerical model

3.1.1. VOF method for air compression/expansion with heat transfer

The flow and heat transfer inside the LP are modeled using FVM (Finite Volume Method) to solve the Navier-Stokes equations coupled with the VOF (Volume Of Fluid) model for the water/air interface tracking. This method has shown its efficiency and adaptability to the modeling of similar flow problems, i.e stratified multi-phase flows with high density ratios [29, 33]. It has been successfully used in our previous study [29] for simulating the LP compression process, showing good agreement with the experimental measurements and capableness of capturing different flow patterns and the conjugated heat transfer behaviors. The same method is therefore used in the present study, for the first time, to simulate the complete CCE cycle using a LP. The governing equations and simulation parameters are presented in detail as below for better understanding of the readers.

The volume fraction of the water α in a cell of the computational grid is given by Eq. 1:

$$\alpha = \frac{V_{water}}{V_{cell}} \tag{1}$$

Where V_{cell} is the volume of the computational cell and V_{water} is the volume of water inside each cell. The viscosity μ and the density ρ of mixture are given by Eq. 2 and Eq. 3, respectively :

$$\mu = \alpha\mu_{water} + (1-\alpha)\mu_{air} \tag{2}$$

$$\rho = \alpha\rho_{water} + (1-\alpha)\rho_{air} \tag{3}$$

The mass conservation equation (the continuity equation) is given by:

$$\frac{\partial \rho}{\partial t} + \nabla \cdot (\rho \mathbf{U}) = 0 \tag{4}$$

where $\mathbf{U}$ is the velocity vector.

The equation expressing conservation of momentum is given by :

$$\frac{\partial \rho \mathbf{U}}{\partial t} + \nabla \cdot (\rho \mathbf{U}\mathbf{U}) - \nabla \cdot (\mu \nabla \mathbf{U}) = \sigma\kappa\nabla\alpha - \mathbf{g}\cdot\mathbf{x}\nabla\rho - \nabla P_d \tag{5}$$

where $\mathbf{g}$ is the gravitational acceleration; $\mathbf{x}$ is the position vector; $\kappa = \nabla \cdot \frac{\nabla \alpha}{|\nabla \alpha|}$ is the curvature of the interface; σ is the surface tension coefficient and $P_d = P - \rho \mathbf{g} \cdot \mathbf{x}$ is the dynamic pressure.

The energy equation is :

$$\frac{\partial \rho T}{\partial t} + \nabla \cdot (\rho \mathbf{U} T) - \nabla \cdot (\mu \nabla T) = - \left(\frac{\alpha}{c_{v,water}} + \frac{1-\alpha}{c_{v,air}} \right) \left(\frac{\partial \rho e_k}{\partial t} + \nabla \cdot (\mathbf{U} e_k) - \nabla \cdot (\mathbf{U} P) \right) \quad (6)$$

where $e_k = \frac{|\mathbf{U}|^2}{2}$ is the specific kinetic energy. $c_{v,water}$ and $c_{v,air}$ are the specific heat capacity at constant volume for the water and air phase, respectively.

The free surface is captured by a transport equation for the water volume fraction :

$$\frac{\partial \alpha}{\partial t} + \mathbf{U} \cdot \nabla \alpha + \nabla \cdot \mathbf{U_r} \alpha (1 - \alpha) = 0 \quad (7)$$

where $\mathbf{U}_r = \mathbf{U}_{water} - \mathbf{U}_{air}$ is the relative velocity vector, also called as the "compression velocity" and $\nabla \cdot \mathbf{U_r} \alpha (1 - \alpha)$ is an anti-diffusion term utilised to sharpen the interface.

3.1.2. Simulation parameters

The transport equations of continuity (mass conservation), momentum and energy are closed by the equations of state for density and enthalpy. The ideal gas law (Eq. 8) is used to model the air. This assumption has been proven to be reasonable for such conditions ($250\,K < T_{air} < 400\,K$ and $10^5 < P < 5 \cdot 10^5$ by other previous studies [25, 34, 11, 15].

$$\rho = \frac{1}{rT} P \quad (8)$$

The viscosity of air $\mu_{air}(T)$ is temperature-dependent and follows the Sutherland equation (Eq. 9) :

$$\mu(T) = \mu_{ref} \frac{T_{ref} + C}{T + C} \left(\frac{T}{T_0} \right)^{\frac{3}{2}} \quad (9)$$

where $T_{ref} = 273.15\,K$ is the reference temperature, $\mu_{ref} = 18.27 \cdot 10^{-6}\,Pa.s$ is the reference viscosity and $C = 110.4$ is the Sutherland coefficient. The thermal conductivity $\lambda_{air} = 0.026\,W.m^{-1}.K^{-1}$ and the heat capacity of air $c_{v,air} = 1.006 \cdot 10^{3}\,J.kg^{-1}.K^{-1}$ are considered as constant in the simulation. For the water phase with almost no temperature change during compression and expansion, constant physical properties at $300\,K$ and $1 \cdot 10^{5}\,Pa$ are used, i.e., $\mu_{water} = 1.005 \cdot 10^{-3}\,kg.m^{-1}.s^{-1}$; $\lambda_{water} = 0.578\,W.m^{-1}.K^{-1}$; $c_{v,water} = 4.184 \cdot 10^{3}\,J.kg^{-1}.K^{-1}$.

OpenFOAM code (version 7) with the *CompressibleInterFoam* solver [35] is used to solve the governing equations. An inlet velocity U_{pist} of water phase is imposed at the bottom boundary of the column while all the other boundaries are treated as isothermal no-slip walls (Fig. 2). The values of $U_{pist} = 0.033\,m.s^{-1}$ for compression and $U_{pist} = -0.033\,m.s^{-1}$ for expansion have been firstly tested, which are identical to those in the experimental study for easy comparison and model validation. The influence of piston speed on the air temperature evolution will be further discussed in section 6 of this paper. Detailed initial and boundary conditions are listed in Table 2.

Variables	Boundary conditions		Initial condition
	Inlet	Wall	Full domain
$U\ (m.s^{-1})$	$U = U_{pist}$ (Dirichlet)	$U_{walls} = 0$ (no-slip)	$U_x = 10^{-5}$, $U_y = 10^{-5}$, $U_z = 10^{-5}$
$P\ (Pa)$	$\frac{\partial P}{\partial n}\|_{\Gamma} = 0$	$\frac{\partial P}{\partial n}\|_{\Gamma} = 0$	101325
$T\ (K)$	(Dirichlet) 300	(Dirichlet) 300	300

Table 2: Boundary and initial conditions for the simulation of air CCE cycle inside the LP column

The Reynolds number of the water and air (Eqs. 10 and 11) during compression and expansion, based on the piston speed $U_{pist} = \pm 0.033\,m.s^{-1}$, are calculated to be $Re_{water} = 1706$ and $Re_{air} = 104$, respectively.

$$Re_{water} = \frac{U_{pist} D}{\nu_{water}} = 1706 \tag{10}$$

$$Re_{air} = \frac{U_{pist} D}{\nu_{air}} = 104 \tag{11}$$

Nevertheless, the local air Re number could be much higher due to the large local air velocities, i.e., increased by a factor of 20 as shown in our previous paper [29]. A turbulence model is thereby necessary to correctly simulate the air compression/expansion by LP [29, 8, 36, 22], especially to capture the appearance of vortices in the flow. In this study, the Large Eddy Simulation (LES) with WALE (Wall Adapting Local Eddy-viscosity) as a sub-grid model is employed. It is the most suitable one for catching and modeling the flow with different regimes and its transition [37].

Simulations are performed under transient-state with adjusted time step. The condition on the time step was linked to Courant number, so that $Co = \frac{u_i \Delta t}{\delta x}$ remains smaller than 1. This condition is necessary for the stability of PISO algorithm [38] which is used for the pressure-velocity coupling [39]. Due to the multiphase flow nature where the VOF method is used for tracking the interface. The interface's Courant number is introduced ($Co_{interface}$) as a critical parameter for the calculation stability. It is recommended that $Co_{interface} < 0.5$ [40, 41]. In our study, it is fixed at $Co_{interface} = 0.35$, therefore, it controls subsequently the time step of Δt, varying from 10^{-4} s to 10^{-3} s.

3.1.3. Mesh convergence study

Grid independence study was firstly conducted to determine the appropriate mesh size and structure for the numerical simulations. Hexahedral mesh has proven its effectiveness and accuracy for this type of geometry and flows in our earlier work [29], thus has been chosen for this study. A structured O-Grid mesh was used (Fig. 3), with mesh refinement at the wall and in the top half of the LP column where air is present during the cooling stage and has the highest temperature and velocity gradients during the compression and expansion. Different mesh sizes have been tested and compared for the convergence

study, with the number of mesh elements increasing from 675 k to 1.4 millions. In order to reduce the computational time, the mesh convergence tests were performed for the first $10\,s$ ($t_e = 10\,s$) of the expansion process, given that the most important evolution of flow patterns happened within this period.

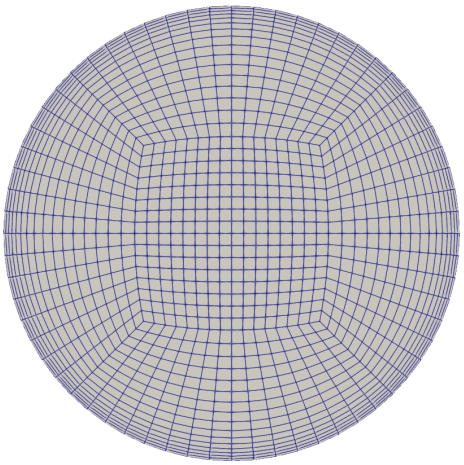

Figure 3: Hexahedral-type mesh with local refining near the wall (O-Grid) used for the simulations

Similar trend on the evolution of the average air temperature ($T_{air,ave}$) can be seen in Fig. 4, except the one with the least number of mesh elements (675 k). The simulation results using this mesh depart significantly from the others from about $t_e = 5\,s$. This is mainly due to the fact that the grid is not enough refined at the near wall regions for which high temperature and velocity gradients could exist. It is therefore estimated that the mesh with 900 k elements is the appropriate one considering both the computational time and the simulation accuracy (deviation smaller than 1% compared to 1.4 million elements). This mesh is then used for the simulation of CCE cycle.

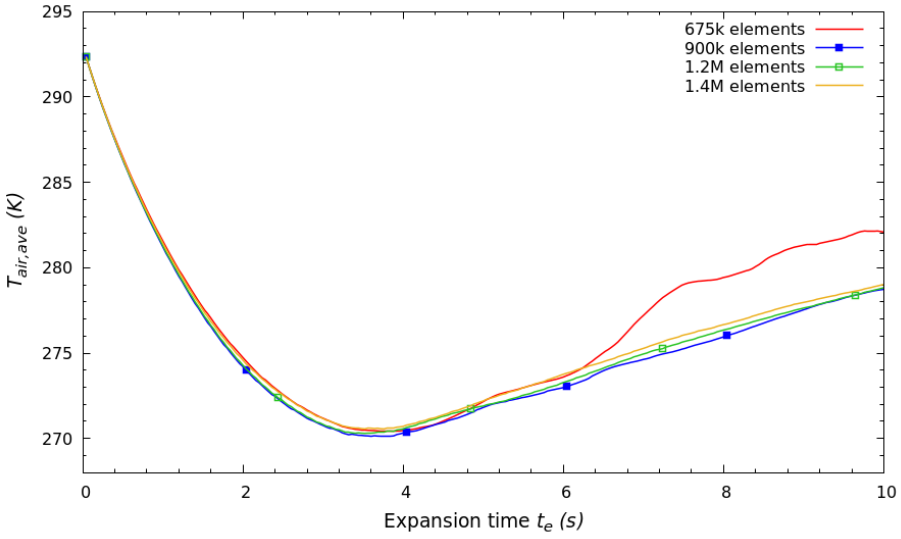

Figure 4: Mesh convergence study: comparison on the evolution of air's average temperature $T_{air,ave}$ over expansion time t_e

3.2. Experimental setup and PIV method

The experimental setup and the PIV visualization technique have been fully developed in our previous experimental study on the air compression [28], and now used in this work for the complete air CCE cycle. Key technical specifications are reported in this sub-section.

The experimental setup (Fig. 5) consists of a vertical piston column, air supply/discharge system and the PIV measurement facility. The cylindrical column is made of transparent material (Borosilicate glass) (3.5 mm in thickness), with an inner diameter of $D = 0.0518\,m$ and a total length larger than L_0. The column is sealed at the top by a plug head and the bottom by a movable (solid) piston with O-ring. Dry air can be injected into and discharged out from the column through the top valves. A pressure sensor (Kistler 4005BA5A) with a measurement range of $5 \cdot 10^5\,Pa$ is also installed on the top to monitor the evolution of air pressure. The piston movement and its speed is controlled by a position controlled electrical actuator, changing the air volume and pressure during the compression and expansion processes. Note that for PIV visual-

ization, the water droplets deposited on the column wall could have a strong disturbance on the measurement. Therefore, the solid piston was used in the experiments to represent the LP concept, given the relatively low piston speed, low compression/expansion ratios (CR and ER) and high length-to-diameter ratio of the column.

The PIV facility is composed of a NDYag laser (532 nm, 15 Hz) with wide flat laser beam lenses and a camera (10 bit 1200 x 1600 pix, FlowSense2ME) in a perpendicular axis (Fig. 5, 6). The camera and the laser were synchronized, capable of simultaneously moving in vertical direction in order to capture images at different column height positions. Di-Ethyl-Hexyl-Sebacat (DEHS) droplets (average diameter of $0.5\,\mu m$) were used as seeding, which were mixed with dry air before entering into the column.

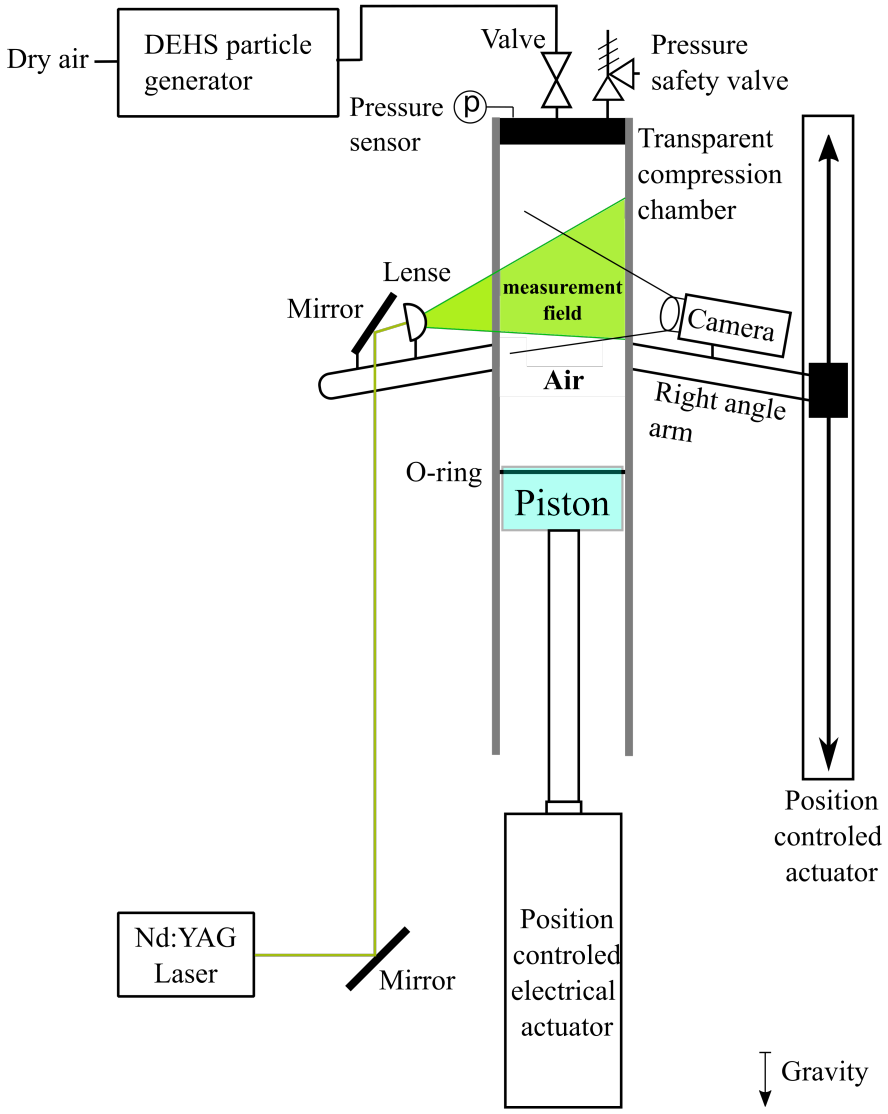

Figure 5: Schematic view of the experimental setup for testing the air CCE cycle. Adapted from [28]

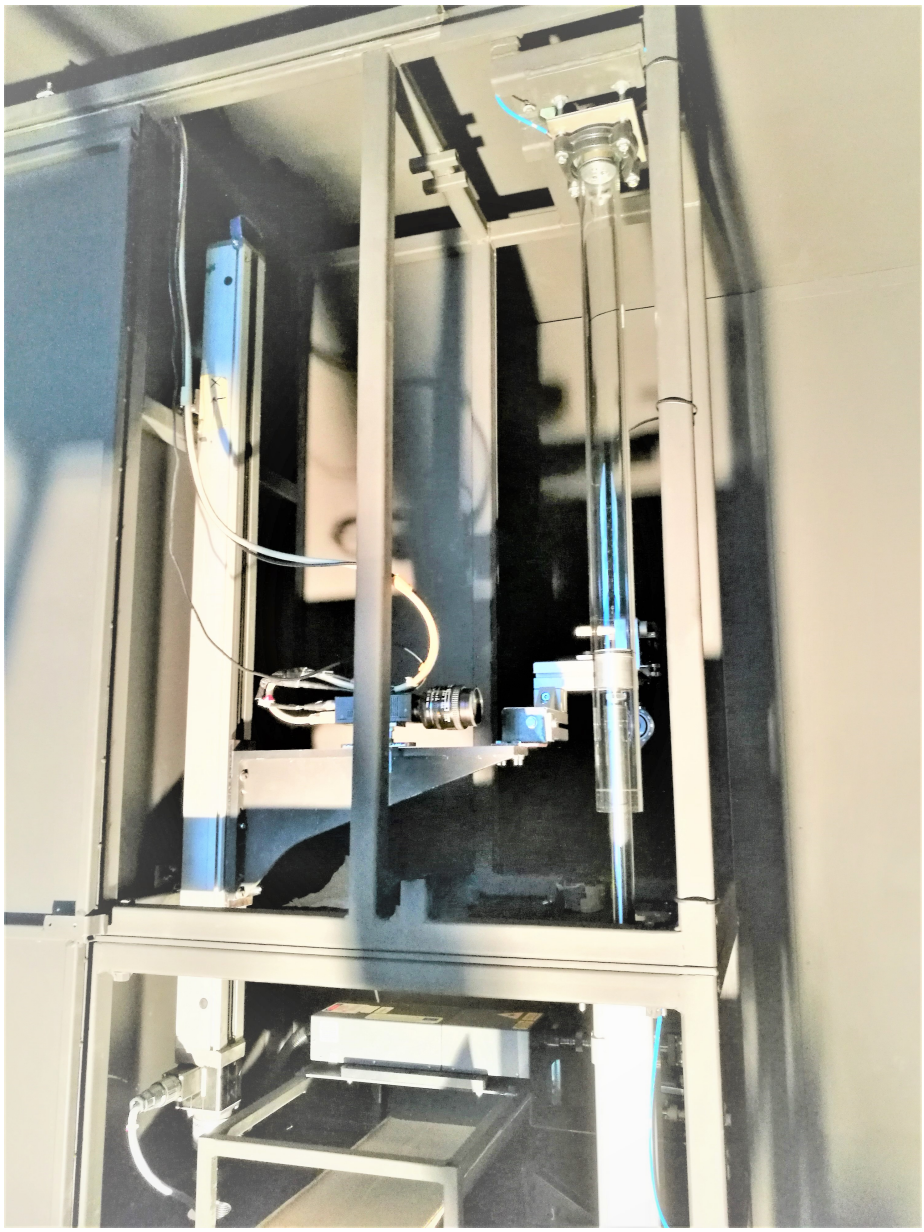

Figure 6: A picture of the experimental setup for testing the air CCE cycle

The positioning was done from an initial point close to the cylinder head in order to generate the admission of particles through the open valve. The valves were then all closed and the test was ready to start. The activation of

the piston and PIV installation were synchronized. The position of the piston, the air pressure in the column and image doublets were also synchronously recorded at a frequency of 15 Hz. The external wall temperature of the column is supposed to be equal to the ambient temperature ($T = 300\ K$).

The whole column length is divided into 10 measurement sections, each containing approximately 100 mm in length, as shown in Figure 7. The CCE cycle has been repeated 10 times to cover all these measurement sections. The obtained images (7750 images during all the CCE cycle) were then processed and connected so as to reconstruct the entire 2D velocity field and its evolution in the piston column. Optical reflections and outside parts were excluded from the data analysis using Matlab script developed in-house. More details about the characterization methodology and the experimental protocol may be found in paper [28].

The air pressure is measured directly by the pressure sensor. Using an inverse method based on the ideal gas law, the air's average temperature $T_{air,ave}$ is calculated by Eq. 12.

$$T = \frac{PV}{mr} = \frac{PVT_0}{P_0V_0} \tag{12}$$

Where V is the volume of the air domain $V = \frac{(L_0 - L_{pist})\pi D^2}{4}$ and r is the ideal gas constant for air.

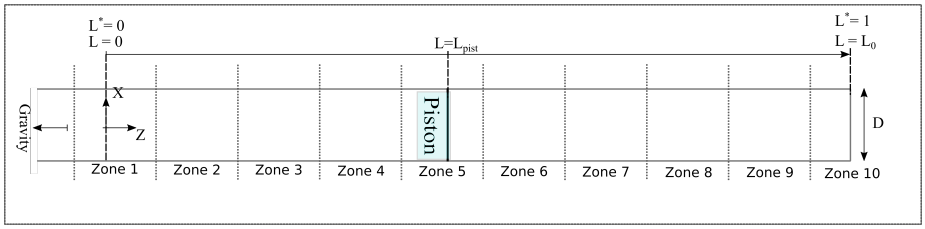

Figure 7: Division of the visualization zones along the Z-direction. Adapted from [28]

3.3. Experimental uncertainties

For the experimental measurements, an uncertainty analysis is conducted.

Quantity	$T_{walls}\,(K)$	$P\,(Pa)$	$D\,(m)$	$L\,(m)$
Range	300-300	$1-5\cdot10^5$	0.906	0.0529
Uncertainty	1	1500	10^{-3}	$2\cdot10^{-3}$

Table 3: Uncertainty of each measured quantity

Using equation 12, the propagation of uncertainties can be calculated as :

$$\frac{\Delta T}{T} = 2\times\frac{\Delta D}{D} + \frac{\Delta P}{P(t)} + \frac{\Delta T_0}{T_0} + \frac{\Delta L}{L(t)} \tag{13}$$

Equation 13 leads to an uncertainty that evolves in time. It can go up to $\frac{\Delta T}{T} = 2.5\%$, which is equal to $\Delta T = 7.5K$ (The uncertainty for the temperature calculation). It should be noted that at the end of the compression, during the cooling and the start of the expansion when the pressures are at their highest levels, a small air leakage may occur due to the use of a solid piston.

3.4. Calculation of efficiencies

Several models are available in the literature for the calculation of compression/expansion efficiencies as well as the overall efficiency of the cycle. They differ from one another by using different paths to calculate the ratio of the energy needed for an isothermal expansion and the one used for the actual compression/expansion. In this study, Yan's model [25] is used for calculating the compression and expansion efficiencies (η_{c+cool} and η_e).

For compression+cooling process:

$$\eta_{c+cool} = \frac{E_p}{W_c} = \frac{(P_c-P_0)V_{iso} + P_0V_0\left(ln(\mathrm{CR}) + \frac{1}{\mathrm{CR}} - 1\right)}{\int_{V_0}^{V_c}(P(t)-P_0)dV + \left(1-\frac{1}{\mathrm{CR}}\right)(P_cV_c - P_0V_0) + (P_c-P_0)V_{iso}} \tag{14}$$

Where W_c is the input work during the compression process, E_p is the total potential energy, V_{iso} is the volume obtained in an isochoric cooling, and CR is the compression ratio ($CR = \frac{P_c}{P_0}$).

For expansion:

$$\eta_e = \frac{W_e}{E_p} = \frac{\int_{V_0}^{V_f}(P(t)-P_f)dV + (P_0-P_f)V_0}{P_0V_0\left(ln(\mathrm{ER})\right) - (P_f(V_{iso}-V_0)) + (P_0-P_f)V_0} \tag{15}$$

Where W_e is the input work during the expansion process, and ER is the expansion ratio $ER = \frac{P_e}{P_f}$.

The overall (Round-trip) efficiency of the cycle can be calculated as:

$$\eta_{cycle} = \eta_{c+cool} * \eta_e \tag{16}$$

4. Comparison between experimental and numerical results for model validation

The obtained simulation results for the studied cycle are firstly compared with the experimental measurements to validate the numerical model. The comparisons are made on both the global and local levels: the evolution of air average temperature and pressure as well as local air velocity profiles and flow patterns.

4.1. Average air pressure and temperature

Figure 8 shows the evolution of air pressure during the CCE cycle, obtained by both CFD simulation and experimental measurement. The air pressure increases from $P_0 \sim 10^5\,Pa$ to $P_c \sim 4.8 \cdot 10^5\,Pa$ during the compression, then slightly drops to $P_{cool} = 4,14 \cdot 10^5\,Pa$ at the end of isochoric cooling. Finally, during the expansion process, it decreases rapidly from P_{cool} to $P_f = 10^5\,Pa$.

Good agreement between the numerical and experimental results can be seen for the pressure evolution. The deviation is smaller than $1.5\,kPa$ for compression and expansion stages while for the cooling stage, a larger gap can be observed ($47\,kPa$).

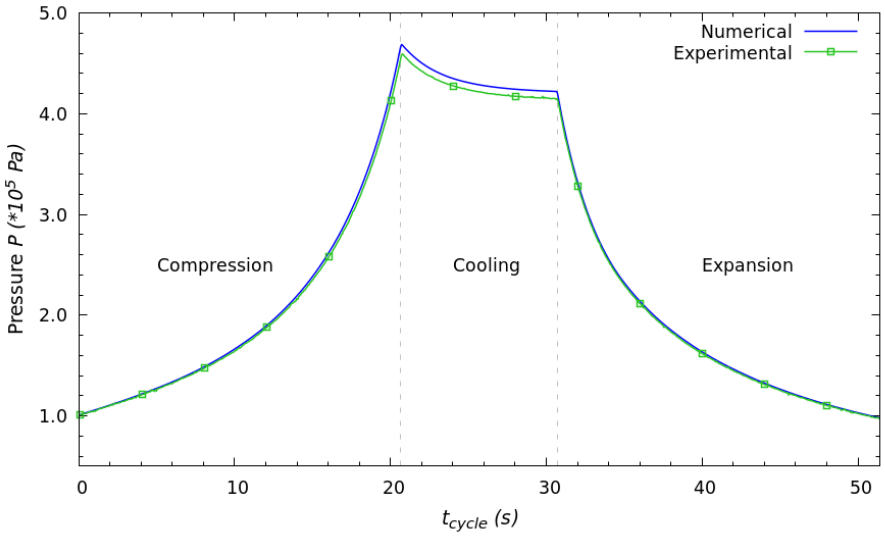

Figure 8: Comparison between experimental and numerical results on the air pressure evolution during the CCE cycle

Figure 9 shows the evolution of $T_{air,ave}$ during the CCE cycle. Good agreement between numerical and experimental results can be found for the compression stage, as has also been observed in our previous study [29]. The air temperature drops then rapidly during the isochoric cooling from T_c to T_{cool}. A discrepancy of $1.5\,K$ may be observed between the numerical and experimental results at the end of cooling (also the beginning of expansion). This is in accordance to the difference in pressure shown in Fig 8. This pressure and temperature difference can be due to the air leakage issue, i.e., a loss of air through safety valve or at the solid piston interface.

For the expansion stage, the air temperature shows a maximum of $\Delta T = 32\,K$ evolution, exhibiting a special trend which is visible in Fig. 9. The $T_{air,ave}$ decreases rapidly first and remains almost constant. The highest gap between numerical and experimental results ($\Delta T = 5.3\,K$ at $t = 33.5\,s$, $t_e = 3.2\,s$) can be found at the turning point of the valley-shape $T_{air,ave}$ curve. At the end of the expansion ($t_e = 20.8\,s$), the air temperature measured experimentally is $3\,K$ lower than the one numerically simulated ($293\,K$).

The experimental uncertainty for $T_{air,ave}$ could unfortunately not be precisely evaluated, due to the fact that it evolves through time and that the temperature is calculated using an inverse method. Despite that, an error margin of $\sigma = \pm 4.1\,K$ has been supposed based on uncertainties of each component (piston position and pressure). The numerical results are basically inside this experimental uncertainty range during all the expansion process except at the transition point where the temperature is at its minimum. While the gap between experimental and numerical results is relatively important for the expansion stage compared to the compression or cooling stage, the similar trend of evolution originated by the physical phenomenon occurred in this stage can be noticed. Further comparison of velocity fields is presented in the next section.

In conclusion, the presented result enabled us to validate the numerical model which will be mainly used for deeper investigation of the flow and heat transfer characteristics.

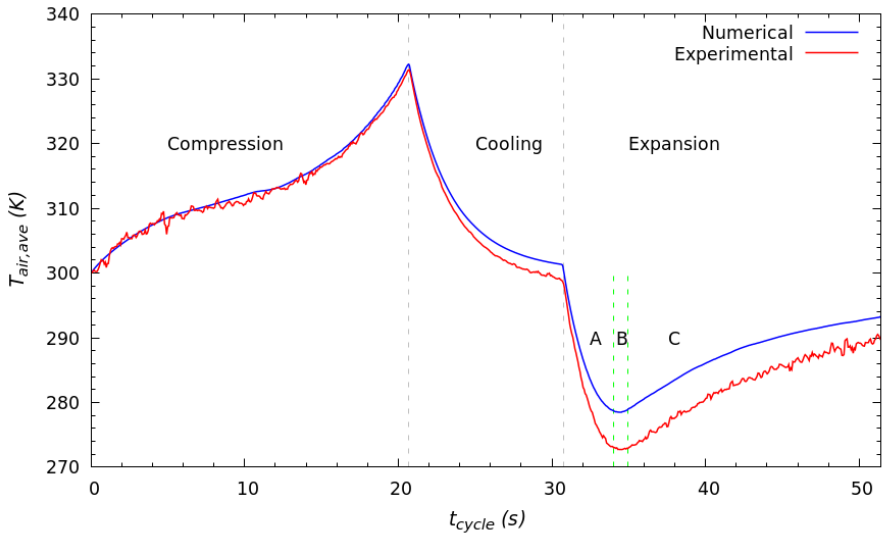

Figure 9: Comparison between experimental and numerical results on the evolution of $T_{air,ave}$ during the CCE cycle

Figure 10 shows the P-V diagram of the air CCE cycle realized by the LP

operation, as well as that for ideal isothermal or adiabatic cycle. The polytropic coefficient for the actual compression and expansion processes is equal to $\gamma_c = 1.09$ and $\gamma_e = 1.012$, respectively, approaching quasi-isothermal operation ($\gamma_c = 1$) rather than the adiabatic cycle ($\gamma = 1.4$). The compression, expansion and overall efficiencies are calculated to be $\eta_{c+cool} = 91.2\%$, $\eta_e = 94.7\%$, and $\eta_{cycle} = 86.9\%$, respectively, highlighting the interests of I-CAES using LP technology.

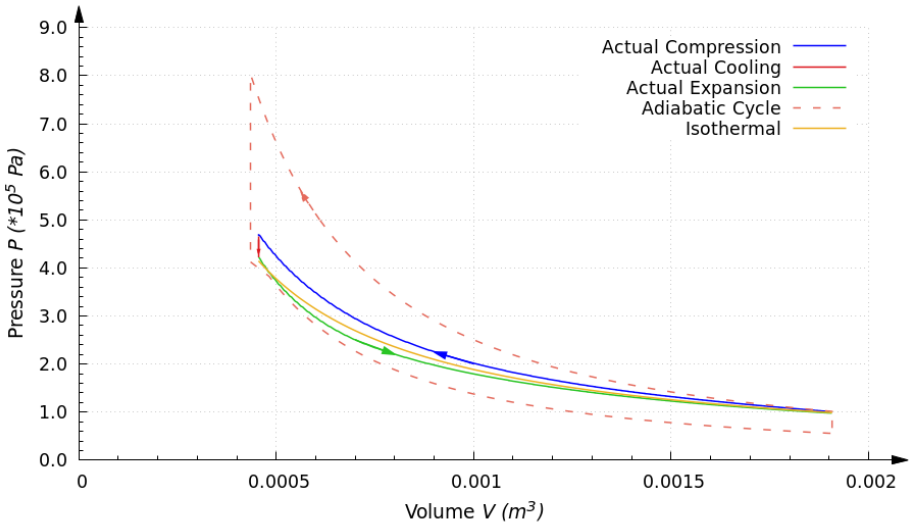

Figure 10: P-V diagram of the tested CCE cycle by LP

4.2. Comparison of local velocity field

The air velocity field obtained by CFD simulation has been compared with the PIV measurement. The compression stage has been addressed in detail in our previous study [29]. The present work is the first that enables a visualisation and comparison of the velocity field during the expansion process captured both experimentally and numerically.

Figure 11 shows a case of established flow structure at $t_e = 2.4\,s$ with very similar axial velocity profiles. In contrast, an agitated flow pattern at $t_e = 9.2s$ is illustrated in Fig. 12, showing clearly the presence of instabilities, swirling flows and vortices. Similar flow pattern is observed both numerically and exper-

imentally, with similar maximum local velocities and with a presence of streamlines in two directions. Various flow patterns and their transitions during the expansion stage will be described in detail in the later section.

In short, the comparison and confrontation between the experimental and CFD results enable us to validate the numerical model (VOF+LES), which will be further used for analyzing the transient flow and heat transfer behaviors during the CCE cycle as well as for evaluating the impact of operation parameters.

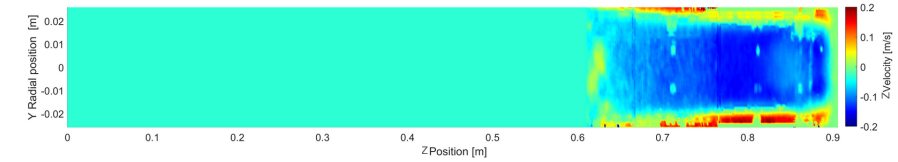

(a) Experimental axial velocity field

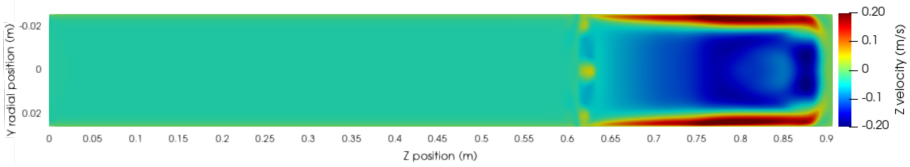

(b) Numerical axial velocity field

Figure 11: Comparison of the axial velocity field between experimental and CFD results at $t_e = 2.4$ s (established flow)

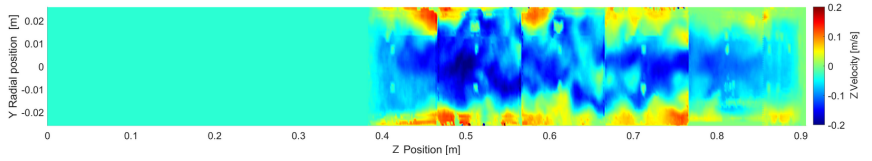

(a) Experimental axial velocity field

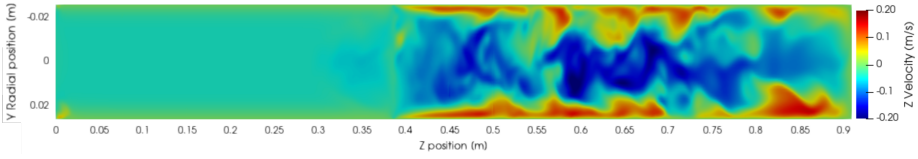

(b) Numerical axial velocity field

Figure 12: Comparison of the axial velocity field between experimental and CFD results at $t_e = 9.2$ s (chaotic flow)

5. Flow and heat transfer characteristics during the CCE cycle

5.1. Compression stage

The flow patterns and heat transfer characteristics during the compression stage of the cycle are rather similar to those presented in [29] thus will not be detailed here. In brief, the compressed air driven by LP advancement undergoes different flow patterns, chronologically from totally axisymmetric flow structure with central ascending-peripheral descending flow in the piston column, to the appearance of smaller ripples and swirls at the interface of rising and falling flows, which then triggers the total dismantling of the main flow structure towards a chaos one. The $T_{air,ave}$ increases continuously from $300\,K$ ($t_c = 0$) to $332\,K$ ($t_c = 20.8\,s$).

5.2. Isochoric cooling stage

The flow patterns and heat transfer during the isochoric cooling stage have not yet been documented before. Therefore, the investigation and analysis are of great interest to understand how it undergoes and to evaluate the impacts on the expansion stage which follows up.

At the beginning of cooling $t_{cool} = 0\,s$ (end of compression), a large temperature gradient up to $70\,K$ exists between the piston interface (cold source) and the column head (hot spots) as show Fig. 13a. The air flow shows strong agitations in the fixed volume due to the inertial effect despite the ceased piston movement (Fig. 14a). This agitated flow pattern helps the heat removal by forced convection through the piston walls and the air-water interface. As a result, the temperature non-uniformity gradually decreases and so does the air velocity magnitude, as shown in Figs. 13b and 14b for $t_{cool} = 4.2\,s$. At the end of the cooling ($t_{cool} = 9.45\,s$), the air is calm down and the velocity field is almost null (Fig. 14c). The air temperature is almost uniform in the column (Fig. 13c), its average value reaching $T_{cool} = 301\,K$ (only 1 K above the initial temperature T_0).

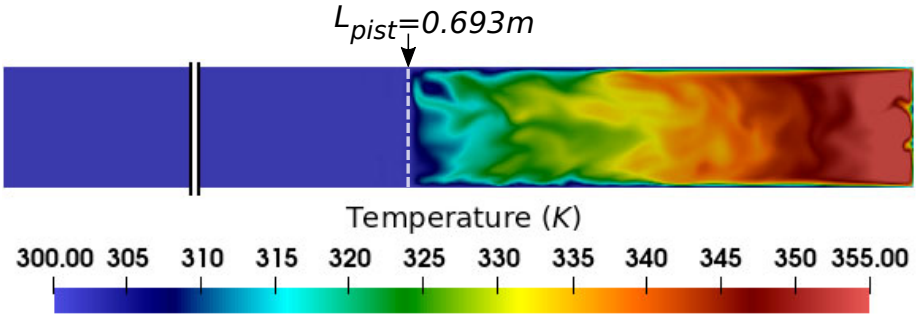

(a) Temperature field at $t = 21.0\,s$, $t_{cool} = 0.2\,s$

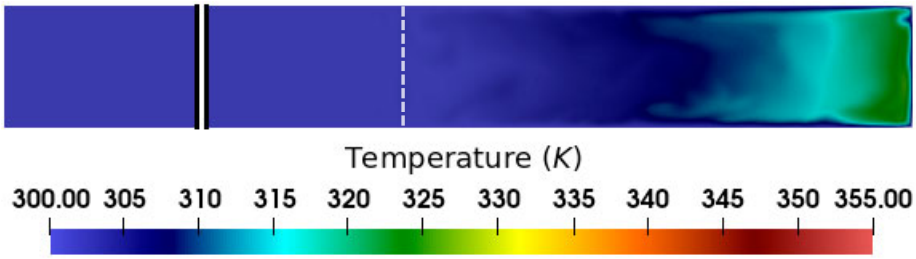

(b) Temperature field at $t = 25.0\,s$, $t_{cool} = 4.2\,s$

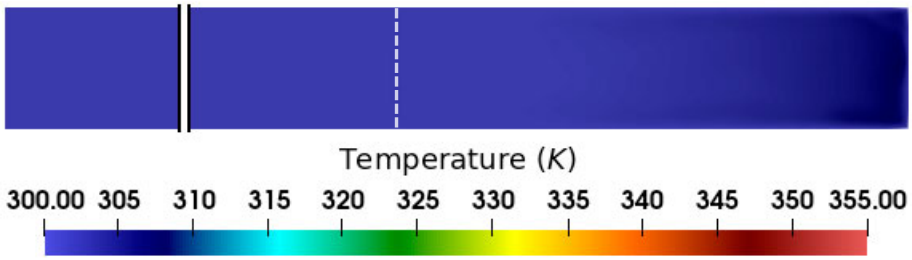

(c) Temperature field at $t = 30.0\,s$, $t_{cool} = 9.45\,s$

Figure 13: Temperature field at $t = 21.0\,s$, $t = 25.0\,s$ and $t = 30.0\,s$ ($t_{cool} = 0.2\,s$, $t_{cool} = 4.2\,s$ and $t_{cool} = 9.45\,s$), respectively

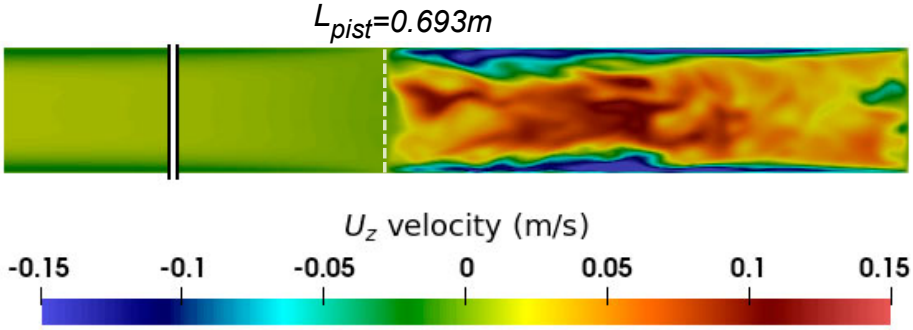

(a) Axial velocity U_z field at $t = 21.0\,s$,$t_{cool} = 0.2\,s$

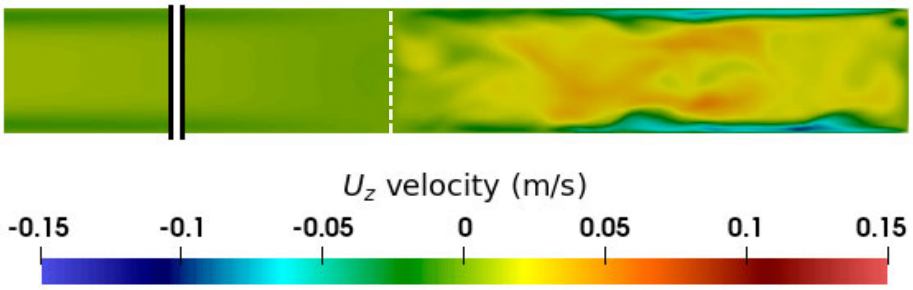

(b) Axial velocity U_z field at $t = 25.0\,s$, $t_{cool} = 4.2\,s$

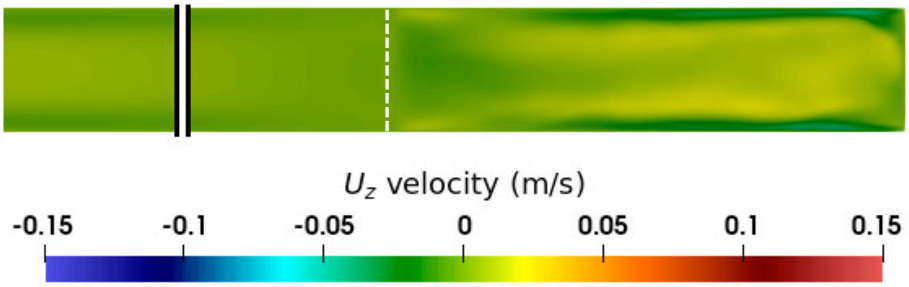

(c) Axial velocity U_z field at $t = 30.0\,s$, $t_{cool} = 9.45\,s$

Figure 14: Axial velocity U_z field at $t = 21.0\,s$, $t = 25.0\,s$ and $t = 30.0\,s$ ($t_{cool} = 0.2\,s$, $t_{cool} = 4.2\,s$ and $t_{cool} = 9.45\,s$), respectively

5.3. Expansion stage

The evolution of $T_{air,ave}$ during the expansion stage can be divided into 3 phases, as shown by the valley curve in Fig. 9:

- (A) Fast and quasi-linear decrease of $T_{air,ave}$ from the beginning of expansion ($t_e = 0$) to $t_e \sim 3.2$ s.

- (B) Almost stagnant air temperature around the lowest point of the valley curve ($3.2\,s < t_e < 4.2\,s$).
- (C) Gradual increase of air temperature until the end of the expansion ($t_e = 21$ s).

The valley shape evolution of $T_{air,ave}$ during the expansion stage is mainly due to the change of its internal energy and the heat exchange with the column walls. As the expansion starts, the decreased air kinetic energy results in a decreased $T_{air,ave}$ (phase A). Meanwhile, due to the downward piston, the contacting surface area between the piston walls and air increases. The augmented heat exchange rate through the piston walls and air-water interface (both at constant temperature of 300 K) by forced convection will then offset the air kinetic energy loss, reaching a short balanced period with stagnant temperature change (phase B). After that, the air is heated up (phase C) due to the relatively small pressure decrease but higher heat absorption owing to the turbulent flow pattern (cf. Fig. 15c) and the still increasing heat transfer area. As a consequence, the final air temperature ($T_f = 293\,K$) at the end of cycle is only $7\,K$ lower than the initial one (T_0).

More information about the local flow and heat transfer characteristics can be obtained by analyzing the air velocity and temperature fields at different phases of air expansion by LP, are shown in Fig. 15 and Fig. 16, respectively.

Shortly after the launch of the expansion (phase A), an axisymmetric flow structure is established (Fig. 15a), characterized by a central descending flow surrounded by a thin layer of ascending air close to the wall. Analogous to the one we discovered for air compression, this specific flow pattern is also originated by the temperature difference between the column center and the near-wall region (Fig. 16a). The warmer and lighter air near the wall would ascend and form the re-circulation. This axisymmetric flow structure evolves over time with larger positive and negative velocities generated ($-7 \times U_{pist} < U_z < 5 \times U_{pist}$). A special velocity and temperature profile can be observed at about $L_z^* = 0.90$ which corresponds to the recirculation zone where cold air

(close to the interface) is in contact with warmer air (close to the piston top), generating some temperature instabilities. The $T_{air,ave}$ continues to decrease, reaching $T_{air,ave} = 279\,K$ at $t_e = 3.2\,s$. Nevertheless, the local values are much lower, i.e., $45\,K$ ($T = 255\,K$) lower than T_0.

Phase B is actually a short transitional regime (1 s) from established flow pattern to disordered one, also corresponding to the lowest point of $T_{air,ave}$ curve. Flow fluctuations can be seen on the velocity field (Fig. 15b), i.e., a high negative velocity zone at $L_z^* = 0.75 - 0.90$ is trapped between air with low velocities. The high positive and negative velocities create a high shear flow which lead to the disruption of the flow structure observed in phase A. A high temperature gradient has been shown near the interface and on the top of the LP chamber (Fig. 16b). The velocity field starts losing its axisymmetric profile and later on, the temperature feature is no more axisymmetric.

The local velocity fluctuations quickly lead to a sudden flow dismantling (Fig. 15c), i.e., the global flow structure is broken into a number of vortices and remains in chaos until the end of expansion (phase C). The central descending-peripheral ascending flow trend can still be recognized, but in an unstable and disordered manner (Fig. 15d). This is mainly due to the heat transfer effect at the column walls, the air temperature starts increasing regularly due to the absorbed heat (Fig. 16c). The temperature distribution becomes more homogeneous at the end of expansion because of the turbulence flow and the the lower difference between air temperatures and the T_{walls} (Fig. 16d) .

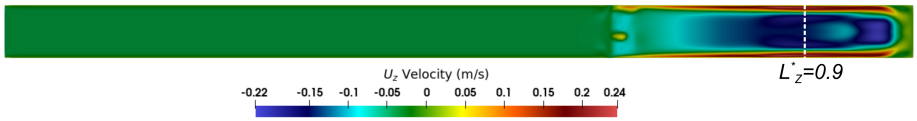

(a) Velocity U_z at $t_e = 2.55\,s$, $(t = 32.95\,s)$ (phase A)

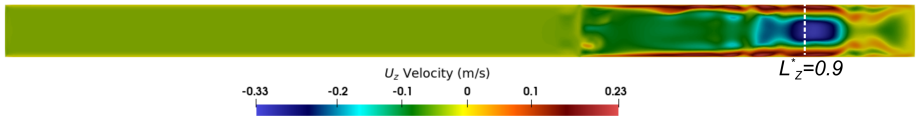

(b) Velocity U_z at $t_e = 3.5\,s$, $(t = 33.9\,s)$ (phase B)

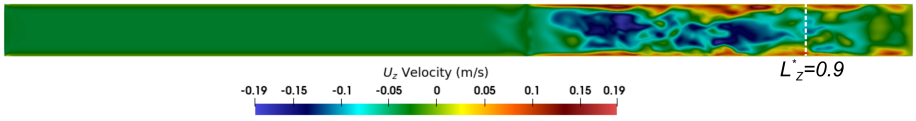

(c) Velocity U_z at $t_e = 5.0\,s$, $(t = 35.4\,s)$ (phase C)

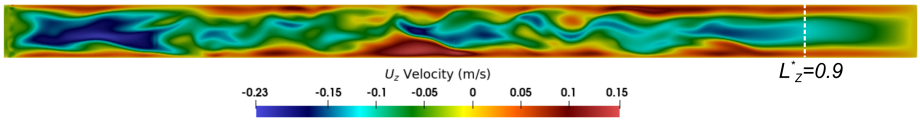

(d) Velocity U_z at $t_e = 20.8\,s = t_f$, $(t = 51,2\,s)$ (phase C, end of expansion)

Figure 15: Velocity field U_z at different expansion times (expansion direction right to left)

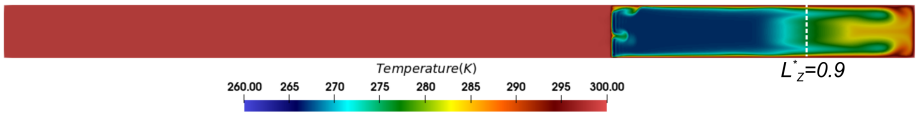

(a) Temperature field T at $t_e = 2.55\,s$ ($t = 32.95\,s$) (phase A)

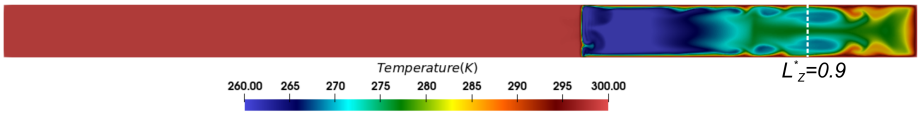

(b) Temperature field T at $t_e = 3.5\,s$, ($t = 33.9\,s$) (phase B)

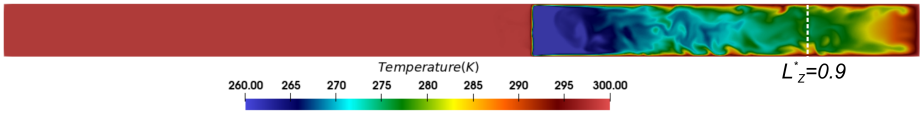

(c) Temperature field T at $t_e = 5.0\,s$, ($t = 35.4\,s$) (phase C)

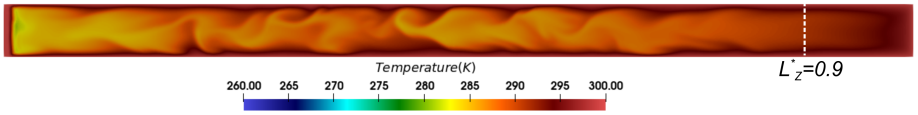

(d) Temperature field T at $t_e = 20.8\,s = t_f$, ($t = 51,2\,s$) (phase C, end of expansion)

Figure 16: Temperature field T at different expansion times (expansion direction right to left)

From Fig. 15 and Fig. 16, it can be seen that the axial position $L_z^* = 0.90$ is the location of interest where high gradients and unique phenomenon occur. Therefore, the axial and radial velocity components (U_x and U_z) and their evolution over expansion time are further plotted to help illustrate different flow patterns and their transition. The established flow structure and its axisymmetric feature in phase A of expansion can be clearly seen, indicated by the overlapped U_z curves at opposite radial positions (Fig. 17) and almost null U_z values shown in Fig. 18. The maximum positive velocities are located at the near wall regions (e.g., $R^* = 0.95$) while the negative maximum velocities are located near the center ($R^* = 0$). The local air velocity keeps increasing during this phase, reaching $U_z = 10 \times U_{pist}$ and $U_z = -7 \times U_{pist}$, respectively.

The recirculation zone evolves in size and moves between $R^* = 0.74$ and $R^* = 0.46$. The U_z velocity component at $R^* = \pm 0.46$ shows strong gradients. A second zone of low or zero velocities is also established for a short time near

the walls. This is coherent to the results shown previously in Fig. 15.

The flow loses its axisymmetry in phase B, indicated by the non-null U_x velocity component on all the radial positions (Fig. 18). The values of U_z component decrease fast during this short transitional period. After that, the U_z velocity shows a rather agitated pattern, fluctuating around half of the maximum positive velocity previously found ($\sim 3 - 5 \times U_{pist}$) close to the piston center ($R^* = 0$) and at negative values ($\sim 2 - 3 \times U_{pist}$) close to the walls (Fig. 17). The radial component U_x also strongly fluctuates and reaches much higher values than in previous phases (Fig. 18).

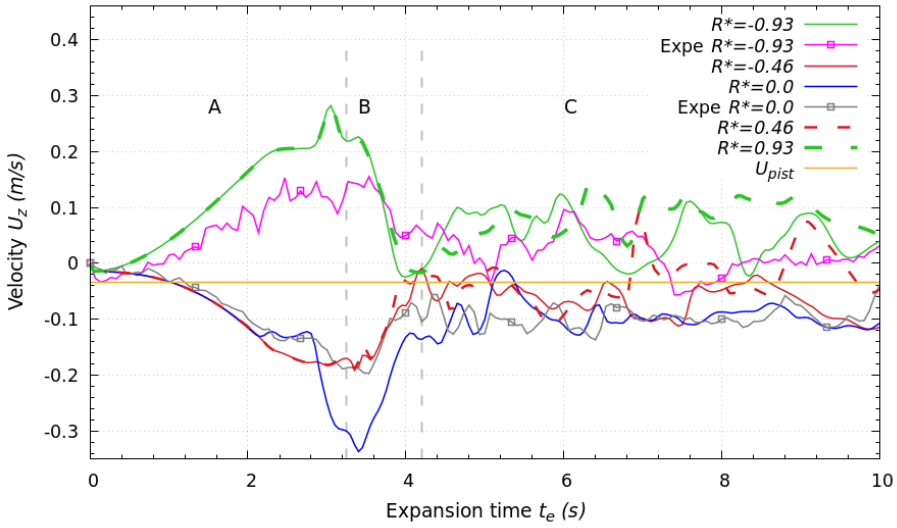

Figure 17: Evolution of local velocity component U_z over expansion time at $L_z^* = 0.90$

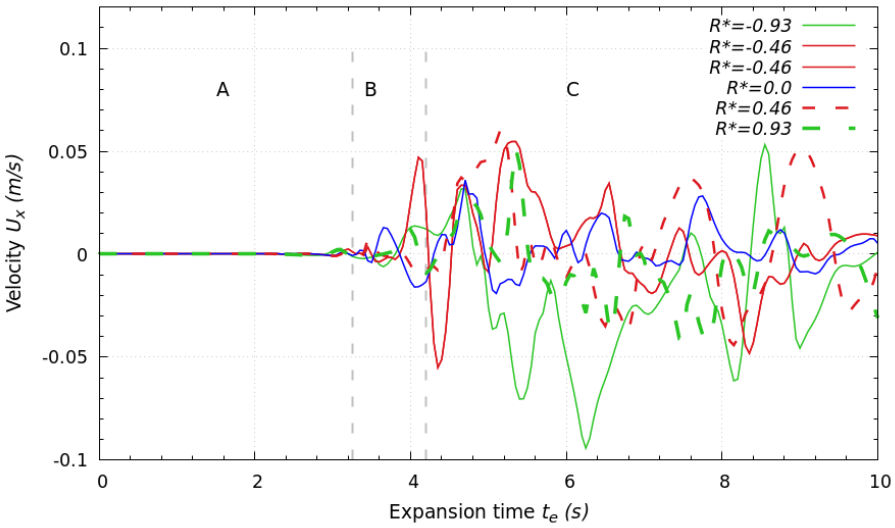

Figure 18: Evolution of local velocity component U_x over expansion time at $L_z^* = 0.90$

6. Effects of operation parameters

In this section, a numerical parametric study is conducted to evaluate the effects of LP operational parameters on the air temperature evolution during the compression and expansion stages as well as on the efficiency.

6.1. Effect of wall temperature

The effect of the external media temperature on the air flow and heat transfer behaviors inside the LP column has not yet been studied in the literature. In reality, as have been reported by Gouda et al. [8], the convection heat transfer between air and walls could be dominant and represent one of the biggest advantages of LP. This effect is evaluated in the present study, by numerically varying the wall temperature from $T_{walls} = 300\,K$ (benchmark case) to $T_{walls} = 293\,K$. Other parameters are kept as the same, as listed in Table 4.

Figure 19 shows the air temperature evolution during compression subjected to different wall temperature. Similar increasing trend can be seen and different phases can be identified (with the same transition moment around $t \sim 10\,s$) for

both wall temperature cases. The same temperature rise of $32\,K$ is recorded due to the air compression by LP at $U_{pist} = 0.033\,m.s^{-1}$. This means that for such LP configuration, the wall (and initial air) temperature has a noticeable but predictable impact on the compression process, due to the forced convective heat transfer being dominant. Lower T_{walls} also results in a slightly higher compression efficiency, i.e., $\eta_c = 91.2\%$ for $T_{walls} = 300\,K$ and $\eta_c = 92.7\%$ at $T_{walls} = 293\,K$ (cf. Table 4).

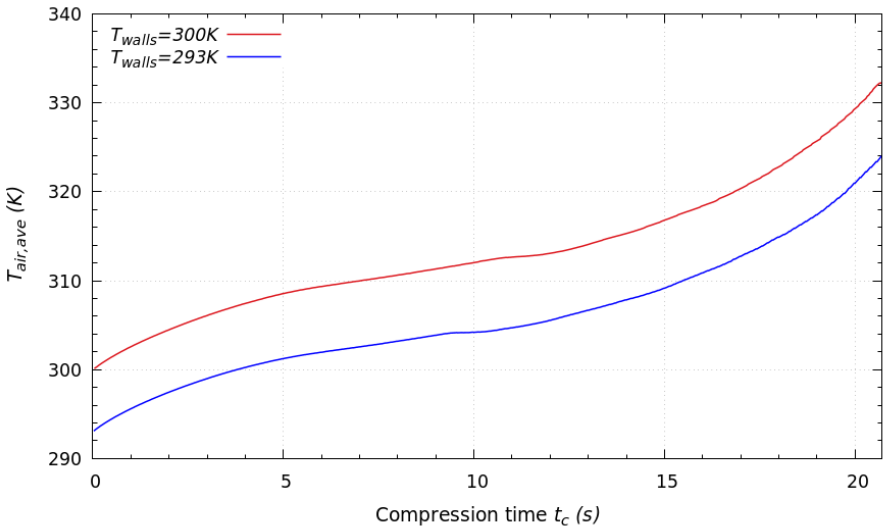

Figure 19: Evolution of $T_{air,ave}$ at different T_{walls} during the compression stage

Figure 20 shows the evolution of $T_{air,ave}$ subjected to different T_{walls} during the expansion stage, analogous to that for the compression stage (Fig. 19). Identical conclusion as that for compression may be drawn because of the same governing heat transfer mechanism (forced convention dominant), i.e., the same transition stages and the same temperature drop (about $8\,K$) before and after the expansion at $U_{pist} = -0.033\,m.s^{-1}$. The expansion efficiency as calculated by Eq. 15 for the two tested T_{walls} values is $\eta_e = 94.7\%$ at $T_{walls} = 300\,K$ and $\eta_e = 95.3\%$ at $T_{walls} = 293\,K$, respectively. Lower environment temperature increases both the compression and expansion efficiencies.

Parameter	$T_{walls} = 293K$	$T_{walls} = 300K$
Initial temperature $T_0\,(K)$	293	300
Operation time (t_c) or $(t_e)\,(s)$	20.8	
Piston speed $U_{pist}\,(m.s^{-1})$	± 0.033	
Final compression $T_{air,ave,c}\,(K)$	325.5	332.7
Compression Efficiency $\eta_c\,\%$	92.7	91.2
Final expansion $T_{air,ave,e}\,(K)$	286.3	293.2
Expansion Efficiency $\eta_e\,\%$	95.3	94.7

Table 4: Effect of wall temperature on the compression and expansion efficiencies of the LP operation. Conditions: $CR = ER = 4.8$; $U_{pist} = +-0.033\,m.s^{-1}$

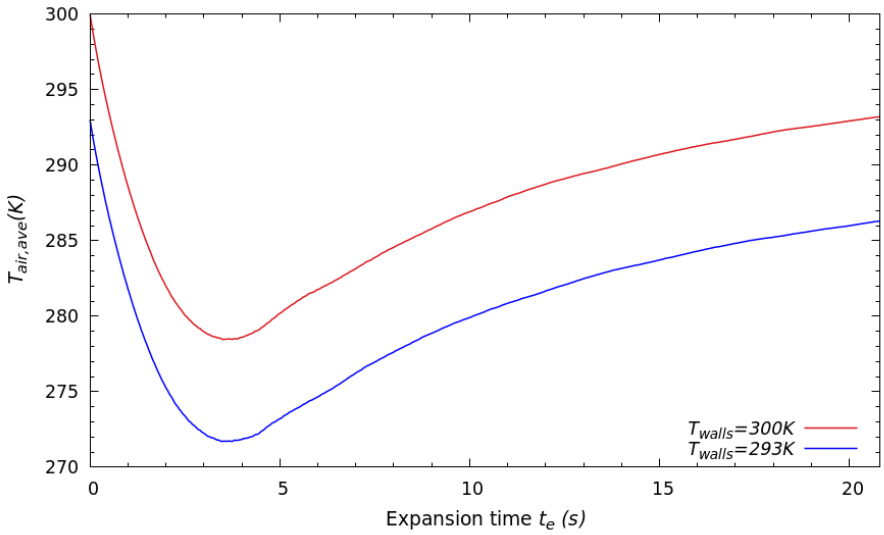

Figure 20: Evolution of $T_{air,ave}$ at different T_{walls} during the expansion stage

6.2. Effect of piston speed

The effect of piston speed on the temperature evolution during the compression stage has been investigated and reported in our previous study [29]. Basically, faster piston speed results in higher temperature rise thus lower compression efficiency as given in Table 5. Similarly, the piston speed has a strong

impact on the air expansion by LP, as shown in Fig. 21. At the same ER and T_{walls}, a temperature drop is established from the beginning of expansion due to different U_{pist}, and it becomes firstly larger then narrowed (valley-shape curve) with the increasing expansion time. More specifically speaking, the air temperature at the end of expansion is only $2\,K$ blow T_0 at the slowest case $U_{pist} = 0.01\,m.s^{-1}$ whereas a final temperature drop of $18\,K$ is registered by fast expansion ($U_{pist} = -0.1\,m.s^{-1}$). The lowest temperature recorded is $T_{air,ave} = 291\,K$ and $T_{air,ave} = 264\,K$, respectively, as shown in Fig. 21. The expansion efficiency also decreases with the increasing piston speed, going from $\eta_e = 97.8\%$ at $U_{pist} = -0.01\,m.s^{-1}$ to $\eta_e = 89.7\%$ at $U_{pist} = -0.1\,m.s^{-1}$.

Configuration	Slow U_{pist}	Ref. study	Fast U_{pist}
Walls temperature $T_{walls}\,(K)$	300		
Piston speed $U_{pist}\,(m.s^{-1})$	± 0.01	± 0.033	± 0.1
Process time (s)	68.6	20.8	6.8
Final compression $T_{air,ave,c}\,(K)$	313.6	332.7	373.9
Compression efficiency $\eta_c\,\%$	97.7	91.2	87
Final expansion$T_{air,ave,e}\,(K)$	297.7	293.2	282.1
Expansion efficiency $\eta_e\,\%$	97.8	94.7	89.7

Table 5: Effect of piston speed on the compression and expansion efficiencies of the LP operation. Conditions: $CR = ER = 4.8$; $T_{walls} = 300\,K$

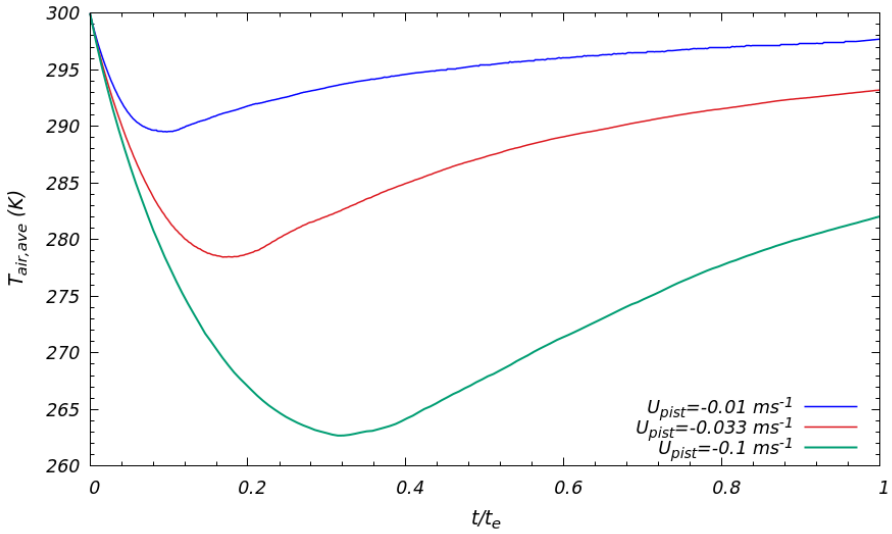

Figure 21: Comparison between air's temperature evolution for three different U_{pist}

As a conclusion, a lower piston speed allows needed time for heat exchange between the air and the walls (the external medium), flattening the variation of air temperature during both the compression and expansion stages, thereby approaching the isothermal operations. For the studied LP configuration ($T_{walls} = 300\,K$ and $U_{pist} = 0.033\,m.s^{-1}$), the overall efficiency is calculated to be $\eta_{cycle} = 87\%$ and can go up to 95.7% at a slower piston speed at $U_{pist} = 0.01\,m.s^{-1}$, highlighting clearly the great interests of LP for I-CAES application.

7. Conclusions and prospects

A complete thermodynamic cycle consisting of air compression-isochoric cooling-expansion (CCE) stages by LP is investigated by means of both CFD simulation and experimental testing in this study. In particular, the transient flow and heat transfer behaviors during different cycle stages have been deeply visualised, compared, analyzed and discussed for the first time. Main conclusions obtained may be listed as follows.

- Numerical and experimental results are in good agreement for the studied cycle, in terms of the evolution of both the air average temperature and pressure. The 3D CFD model using VOF method for interface tracking with LES turbulence model is confirmed to be capable of capturing the specific flow patterns and their transition inside the LP column, constituting thereby a useful tool to acquire better understanding of the flow and heat transfer mechanisms occurred during the LP cycle operation.

- Flow and heat transfer behaviors during the Isochoric cooling process show calm flow and almost homogeneous temperature could be achieved within a short period of time ($t_{cool} = 9.45\,s$).

- The evolution of air average temperature shows a valley-type curve during the expansion stage, corresponding to three phases with distinguished flow patterns and heat transfer characteristics. An axisymmetric flow structure with central descending-peripheral ascending flow is established during the first seconds of expansion, accompanied by a rapid decrease of air temperature due to the loss of kinetic energy. A short transition period comes after with almost unchanged air temperature, during which the global flow structure is totally destroyed into a multitude of small vortices. The chaotic flow patterns lasts till the end of expansion with smooth increase of air temperature mainly due to the heating from the column walls.

- Such air CCE cycle realized by LP can approach the near isothermal operation, with a polytropic exponent of $\gamma_c = 1.09$ and $\gamma_e = 1.012$, respectively. The efficiency for the compression, expansion and overall cycle is calculated to be $\eta_c = 91.2\%$, $\eta_e = 94.7\%$, and $\eta_{cycle} = 86.9\%$ ($U_{pist} = 0.033\,m.s^{-1}$; $T_{walls} = 300\,K$ and $CR = ER = 4.8$), showing great interest for I-CAES application by LP.

- The results of a numerical parametric study show that both the wall (and initial air) temperature and the piston speed have effects on the air tem-

perature evolution and on the efficiencies. The impact of T_{walls} is noticeable and predictable at the given U_{pist} due to the fact that the forced convection dominants the heat transfer. A lower T_{walls} value augments slightly both the compression and expansion efficiencies. Regarding the U_{pist}, a fast compression/expansion results in a larger variation of air temperature, thus lower efficiency. A slow piston speed leaves more time for cooling or heating of the air by column walls, thus beneficial to reach high overall efficiencies (up to $\eta_e = 97.9\%$, $\eta_c = 97.7\%$ and $\eta_{cycle} = 95.6\%$ at $U_{pist} = 0.01\, m.s^{-1}$).

The present study enabled us to have a complete numerical model and experimental setup to investigate the flow and heat transfer inside LP compression chamber. This numerical model can be used to investigate the effects of the presence of physical walls of the piston column on the flow and heat transfer characteristics of the compressed air. Moreover, the structuring of the LP walls to further approach the isothermal cyclic operation is our on-going work, by coupling the CFD model with some shape or topology optimization methods.

8. Acknowledgement

This work is supported by the French *Association Nationale de la Recherche et de la Technologie* (ANRT) under the CIFRE program No. 2017/1100 and by *France Relance* recovery plan of French state of 21 December 2020 within the framework of the project *CNRS-SEGULA*.

References

[1] BP, BP energy outlook 2022, Tech. Rep. 9, BP (2022).
URL `https://www.bp.com/content/dam/bp/business-sites/en/global/corporate/pdfs/energy-economics/energy-outlook/bp-energy-outlook-2022.pdf`

[2] IEA, Renewable Energy Market Update - May 2022, IEA, Paris, Tech. rep., IEA (2022).
URL https://www.iea.org/reports/renewable-energy-market-update-may-2022

[3] E. Bazdar, M. Sameti, F. Nasiri, F. Haghighat, Compressed air energy storage in integrated energy systems: A review, Renewable and Sustainable Energy Reviews 167 (2022) 112701. doi:10.1016/J.RSER.2022.112701.

[4] H. Wang, Z. Wang, C. Liang, R. Carriveau, D. S. K. Ting, P. Li, H. Cen, W. Xiong, Underwater Compressed Gas Energy Storage (UWCGES): Current Status, Challenges, and Future Perspectives, Applied Sciences 2022, Vol. 12, Page 9361 12 (18) (2022) 9361. doi:10.3390/APP12189361.

[5] J. Bai, W. Wei, L. Chen, S. Mei, Modeling and dispatch of advanced adiabatic compressed air energy storage under wide operating range in distribution systems with renewable generation, Energy 206 (2020) 118051. doi:10.1016/J.ENERGY.2020.118051.

[6] A. G. Olabi, T. Wilberforce, M. Ramadan, M. A. Abdelkareem, A. H. Alami, Compressed air energy storage systems: Components and operating parameters – A review, Journal of Energy Storage 34 (2021) 102000. doi:10.1016/J.EST.2020.102000.

[7] L. Chen, L. Zhang, Y. Wang, M. Xie, H. Yang, K. Ye, S. Mohtaram, Design and performance evaluation of a novel system integrating Water-based carbon capture with adiabatic compressed air energy storage, Energy Conversion and Management 276 (2023) 116583. doi:10.1016/J.ENCONMAN.2022.116583.

[8] E. M. Gouda, Y. Fan, M. Benaouicha, T. Neu, L. Luo, Review on Liquid Piston technology for compressed air energy storage, Journal of Energy Storage 43 (2021) 103111. doi:10.1016/j.est.2021.103111.

[9] V. C. Patil, P. Acharya, P. I. Ro, Experimental investigation of heat transfer

in liquid piston compressor, Applied Thermal Engineering 146 (2019) 169–179. doi:10.1016/j.applthermaleng.2018.09.121.

[10] Q. Zhou, D. Du, C. Lu, Q. He, W. Liu, A review of thermal energy storage in compressed air energy storage system, Energy 188 (2019) 115993. doi:10.1016/j.energy.2019.115993.

[11] J. D. Van de Ven, P. Y. Li, Liquid piston gas compression, Applied Energy 86 (10) (2009) 2183–2191. doi:10.1016/j.apenergy.2008.12.001.

[12] T. Neu, Device and method for converting and storing electric energy in the form of compressed air (12 2016).
URL https://patentscope.wipo.int/search/en/detail.jsf?docId=WO2016193322

[13] O. Maisonnave, L. Moreau, R. Aubrée, M. F. Benkhoris, T. Neu, D. Guyomarc'h, Optimal energy management of an underwater compressed air energy storage station using pumping systems, Energy Conversion and Management 165 (2018) 771–782. doi:10.1016/j.enconman.2018.04.007.

[14] M. Khaljani, J. Harrison, D. Surplus, A. Murphy, P. Sapin, C. N. Markides, Y. Mahmoudi, A combined experimental and modelling investigation of an overground compressed-air energy storage system with a reversible liquid-piston gas compressor/expander, Energy Conversion and Management 245 (2021) 114536. doi:10.1016/J.ENCONMAN.2021.114536.

[15] A. Odukomaiya, A. Abu-Heiba, K. R. Gluesenkamp, O. Abdelaziz, R. K. Jackson, C. Daniel, S. Graham, A. M. Momen, Thermal analysis of near-isothermal compressed gas energy storage system, Applied Energy 179 (2016) 948–960. doi:10.1016/j.apenergy.2016.07.059.

[16] A. Odukomaiya, A. Abu-Heiba, S. Graham, A. M. Momen, Experimental and analytical evaluation of a hydro-pneumatic compressed-air Ground-Level Integrated Diverse Energy Storage (GLIDES) system, Applied Energy 221 (2018) 75–85. doi:10.1016/j.apenergy.2018.03.110.

[17] C. Zhang, J. H. Wieberdink, T. W. Simon, P. Y. Li, J. D. Van de Ven, E. Loth, Numerical analysis of heat exchangers used in a liquid piston compressor using a one-dimensional model with an embedded two-dimensional submodel, in: ASME International Mechanical Engineering Congress and Exposition, Proceedings (IMECE), Vol. 8A, ASME, 2014, p. V08AT10A095. doi:10.1115/IMECE2014-38567.

[18] G. Dib, P. Haberschill, R. Rullière, R. Revellin, Thermodynamic investigation of quasi-isothermal air compression/expansion for energy storage, Energy Conversion and Management 235 (2021) 114027. doi:10.1016/j.enconman.2021.114027.

[19] V. C. Patil, J. Liu, P. I. Ro, Efficiency improvement of liquid piston compressor using metal wire mesh for near-isothermal compressed air energy storage application, Journal of Energy Storage 28 (2020) 101226. doi:10.1016/j.est.2020.101226.

[20] V. C. Patil, P. I. Ro, Experimental study of heat transfer enhancement in liquid piston compressor using aqueous foam, Applied Thermal Engineering 164. doi:10.1016/j.applthermaleng.2019.114441.

[21] B. Ahn, V. C. Patil, P. I. Ro, Effect of Integrating Metal Wire Mesh with Spray Injection for Liquid Piston Gas Compression, Energies 2021, Vol. 14, Page 3723 14 (13) (2021) 3723. doi:10.3390/EN14133723.

[22] C. Zhang, P. Y. Li, J. D. Van De Ven, T. W. Simon, Design analysis of a liquid-piston compression chamber with application to compressed air energy storage, Applied Thermal Engineering 101 (2016) 704–709. doi:10.1016/j.applthermaleng.2016.01.082.

[23] A. Török, S. Petrescu, G. Popescu, M. Feidt, Quasi-Izothermal Compressors And Expanders With Liquid Piston, Termotehnica (2013) 9.

[24] C. Zhang, T. W. Simon, P. Y. Li, J. D. Van De Ven, Numerical modeling of three-dimensional heat transfer and fluid flowthrough interrupted plates

using unit cell scale, Special Topics and Reviews in Porous Media 6 (2) (2015) 145–158. doi:10.1615/.2015012321.

[25] B. Yan, J. H. Wieberdink, F. A. Shirazi, P. Y. Li, T. W. Simon, J. D. Van de Ven, Experimental study of heat transfer enhancement in a liquid piston compressor/expander using porous media inserts, Applied Energy 154 (2015) 40–50. doi:10.1016/j.apenergy.2015.04.106.

[26] J. Wieberdink, P. Y. Li, T. W. Simon, J. D. Van de Ven, Effects of porous media insert on the efficiency and power density of a high pressure (210 bar) liquid piston air compressor/expander : An experimental study, Applied Energy 212 (2018) 1025–1037. doi:10.1016/j.apenergy.2017.12.093.

[27] C. Li, H. Wang, X. He, Y. Zhang, Experimental and thermodynamic investigation on isothermal performance of large-scaled liquid piston, Energy 249 (2022) 123731. doi:10.1016/J.ENERGY.2022.123731.

[28] T. Neu, A. Subrenat, Experimental investigation of internal air flow during slow piston compression into isothermal compressed air energy storage, Journal of Energy Storage 38 (2021) 102532. doi:10.1016/j.est.2021.102532.

[29] E. M. Gouda, M. Benaouicha, T. Neu, Y. Fan, L. Luo, Flow and heat transfer characteristics of air compression in a liquid piston for compressed air energy storage, Energy 254 (2022) 124305. doi:10.1016/J.ENERGY.2022.124305.

[30] Y. M. Kim, D. Favrat, Energy and exergy analysis of a micro-compressed air energy storage and air cycle heating and cooling system, Energy 35 (1) (2010) 213–220. doi:10.1016/j.energy.2009.09.011.

[31] Q. Yu, X. Li, Y. Geng, X. Tan, Study on quasi-isothermal expansion process of compressed air based on spray heat transfer, Energy Reports 8 (2022) 1995–2007. doi:10.1016/j.egyr.2022.01.019.

[32] M. Z. Getie, F. Lanzetta, S. Bégot, B. T. Admassu, A. A. Hassen, Reversed regenerative Stirling cycle machine for refrigeration application: A review, International Journal of Refrigeration 118 (2020) 173–187. doi:10.1016/J.IJREFRIG.2020.06.007.

[33] S. Mirjalili, S. S. Jain, M. S. Dodd, Interface-capturing methods for two-phase flows : An overview and recent developments, Center for Turbulence Research: Annual Research Briefs 1 (2017) 117–135. doi:http://dx.doi.org/10.1080/10304312.2017.1409340.

[34] B. Yan, T. Simon, P. Li, Compression/expansion within a cylindrical chamber: Application of a liquid piston and various porous inserts, Ph.D. thesis, University of Minnesota (2013).

[35] The OpenFOAM Foundation, OpenFOAM — Free CFD Software — The OpenFOAM Foundation.
URL https://openfoam.org/

[36] E. M. Gouda, M. Benaouicha, T. Neu, P. Vergnol, F. Yilin, L. Luo, 2D versus 3D numerical modeling of flow and heat transfer in a liquid piston air compressor, in: ICNAAM 2021 19th International Conference Of Numerical Analysis And Applied Mathematics, Rhodes, Greece, 2021, p. XX.

[37] F. Nicoud, F. Ducros, Subgrid-Scale Stress Modelling Based on the Square of the Velocity Gradient Tensor, Flow, Turbulence and Combustion 62 (3) (1999) 183–200. doi:10.1023/A:1009995426001.

[38] R. I. Issa, Solution of the implicitly discretised fluid flow equations by operator-splitting, Journal of Computational Physics 62 (1) (1986) 40–65. doi:10.1016/0021-9991(86)90099-9.

[39] J. H. Ferziger, M. Perić, Computational Methods for Fluid Dynamics, Computational Methods for Fluid Dynamicsdoi:10.1007/978-3-642-56026-2.

[40] S. S. Deshpande, L. Anumolu, M. F. Trujillo, Evaluating the performance of the two-phase flow solver interFoam, Computational Science and Discovery 5 (1) (2012) 14016. doi:10.1088/1749-4699/5/1/014016.

[41] J. Roenby, H. Bredmose, H. Jasak, A computational method for sharp interface advection, Royal Society Open Science 3 (11). doi:10.1098/RSOS.160405.